PERGAMON

International Journal of Solids and Structures 39 (2002) 3543–3554

INTERNATIONAL JOURNAL OF SOLIDS and STRUCTURES

www.elsevier.com/locate/ijsolstr

Microstructures and interfaces in Ni–Al martensite: comparing HRTEM observations with continuum theories

Dominique Schryvers [a,*], Philippe Boullay [a,1], Pavel L. Potapov [a], Robert V. Kohn [b], John M. Ball [c]

[a] *EMAT, University of Antwerp, RUCA, Groenenborgerlaan 171, B-2020 Antwerp, Belgium*
[b] *Courant Institute of Mathematical Sciences, 251 Mercer Street, New York, NY 10012, USA*
[c] *Mathematical Institute, University of Oxford, St-Giles 24-29, Oxford OX1 3LB, UK*

Received 1 August 2001; received in revised form 2 October 2001

Abstract

Different microstructural configurations of Ni–Al martensite are described on the meso- and atomic-scale, based on transmission electron microscopy images at conventional and atomic resolution. The observed structural features are described in close correlation with modern linear and non-linear continuum models, explaining the existence of particular orientations and stress accommodating features such as lattice reorientation, twin tapering and bending.

Keywords: Martensite; Ni–Al; HRTEM; Continuum theory; Microstructure

1. Introduction

Intermetallic Ni–Al compounds with a composition in the range between 42 and 70 at.% Ni attract much attention due to a unique combination of a high melting point, a low density and a high oxidation resistance. Moreover, like many other B2 compounds, Ni-rich Ni–Al (with about 62–69 at.% Ni) undergoes a diffusionless cubic-to-tetragonal martensitic transformation on cooling. The resulting structure is usually described in terms of the $L1_0$ ordering and forms multiply twinned martensite plates (Baele et al., 1987; Chakravorty and Wayman, 1976; Schryvers, 1993). Each twin variant can be regarded as one deformation variant in the cubic-to-tetragonal description of this transformation, as shown in Fig. 1. On heating, the B2 structure is restored by the reverse transformation yielding shape memory behaviour.

The formation of multiply twinned martensite plates or combinations of such plates is governed by the accommodation of the shape change and minimisation of the elastic energy. Each plate consists of two of the three possible deformation variants U_1, U_2 and U_3 described by the diagonal matrix (η_1, η_1, η_3) and

* Corresponding author. Fax: +32-3-2180-257.
E-mail address: schryver@ruca.ua.ac.be (D. Schryvers).
[1] Now at SPCTS, Limoges, France.

0020-7683/02/$ - see front matter
PII: S0020-7683(02)00167-1

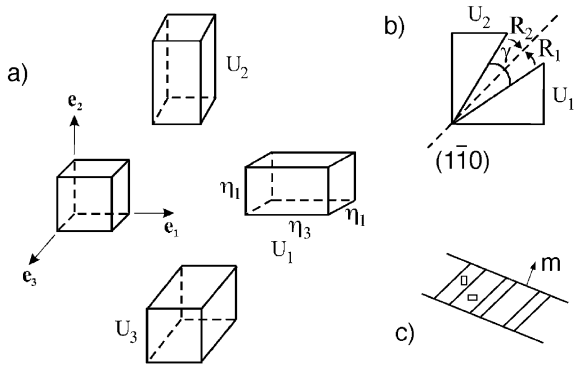

Fig. 1. Schematic of the cubic-to-tetragonal transformation showing (a) the different deformation variants, (b) the combination of two variants around a microtwin plane (2D projection) and (c) the configuration of a microtwinned plate.

permutations hereof, where $\eta_1 < 1 < \eta_3$. The microtwin planes inside these martensite plates are close packed $\{1\,1\,1\}$ type planes in the $L1_0$ description of the martensite structure and they originate from former $\{1\,1\,0\}$ type planes of the B2 austenite. In compositions with less than 63 at.% Ni, the martensite has a fine periodical microtwin structure (Martynov et al., 1983; Schryvers and Tanner, 1991) with a typical stacking period of seven close packed layers in a $(5\bar{2})$ sequence and denoted as 14M (Otsuka et al., 1993) (formerly referred to as 7R or 7M). Occasionally, other stacking sequences, such as a 10 layered stacking have been observed (Chandrasekaran et al., 1992). Within the concept of minimisation of the elastic energy the numerical values of the deformation parameters dictate the final volume fractions λ, rigid body rotations R_i, habit plane normals m_i, etc. When the transformation proceeds, each plate will continue to grow and finally martensite–martensite interfaces will be formed. When disregarding local differences in microtwin sequences, such interfaces can be referred to as macrotwin planes. Although interfaces between different martensite plates resulting from this type of transformation have been investigated before (Baele et al., 1987; Chakravorty and Wayman, 1976), no detailed study on the atomic configurations at these interfaces has been conducted so far for Ni–Al. It is clear that the local atomic structure of the interfaces could play an important role in the reversibility and thus the shape memory behaviour of these materials.

In the present paper an overview of different micro- and nanoscale configurations of martensite microstructures and martensite–martensite interfaces in Ni–Al as observed in different transmission electron microscopy (TEM) modes will be presented. A variety of different configurations is obtained by applying different materials preparation methods, particularly by altering the cooling rate and solidification conditions. It will be shown that local stress and composition conditions can play an important role in the final structures appearing. The formed interfaces will depend on the original choice of deformation variants, the actual orientation of the microtwin planes and the stability of the volume fractions on either side. Experimental measures and typical configurations are compared with theoretical predictions from continuum theories.

2. Experiment

Ni–Al bulk material with a Ni content of 65 at.% Ni, further referred to as 65Ni, was prepared in the form of ingots by arc melting starting from 99.99% pure elements. The ingots are homogenised by annealing for 1 h at 1250 °C, followed by a water quench. Ni–Al splat-cooled samples of the same composition were prepared by pressing a free falling droplet of the melt in between two copper pistons that are

shot against each other with a velocity of 8 m/s (Schryvers and Holland-Moritz, 1998). The solidification of the melt results from the heat transfer occurring during the contact of the pistons with the melt. A cooling rate of approximately 9×10^5 K/s is obtained. The resulting discs have a diameter of approximately 20 mm and a thickness of about 200 μm. Melt-spun Ni–Al ribbons, again with the same composition, were prepared by the single-roller melt-spinning technique with a cooling rate between 10^5 and 10^6 K/s (Potapov et al., 2000).

From bulk, splat-cooled as well as melt-spun samples, 3 mm diameter discs suitable for observations in TEM were obtained. These discs were then thinned by the double-jet electropolishing technique using a Struers Tenupol-3 instrument (Schryvers and Tanner, 1990).

Selected area electron diffraction (SAED) and low magnification observations were carried out using a Philips CM20 Twin microscope, allowing large tilting angles along two perpendicular axes. This instrument is also equipped with an energy dispersive X-ray (EDX) analysis detector, yielding compositional information of small regions. The high-resolution transmission electron microscopy (HRTEM) images were recorded on a JEOL 4000EX top-entry microscope. Both instruments are equipped with a LaB_6 filament, providing a coherent electron beam necessary for HRTEM work. Supporting electron energy loss spectroscopy (EELS) was performed on a CM30 instrument equipped with a Gatan imaging filter and a field-emission gun for high brightness and coherency.

3. Results

In the present contribution, the results of the covered studies are organised per material preparation technique. First some particular martensite microstructures observed in splat-cooled samples are presented, followed by evidence for nanoscale multistructural phases observed in melt-spun material. Finally, atomic-scale detail of martensite–martensite interfaces in bulk samples is shown and discussed.

3.1. Splat-cooled material

Splat-cooled 65Ni material is nearly completely transformed into martensite at room temperature with only a few retained B2 grains. Some grains are fully transformed into a single microtwinned martensite plate, i.e., with one family of microtwin planes, while others reveal different microtwinning planes. An example of the latter is shown in Fig. 2a, showing irregular microtwinning. Indeed, in the lower-right part a fine and a broad sequence are observed while in the upper-left part broad untwinned regions alternating with fine twinning are found. Moreover, the interface (running between the two arrows) between both parts in Fig. 2a has a stairway configuration with steps parallel with one of the microtwin planes (always the one in the lower-right part), i.e., a former $(1\,1\,0)_{B2}$ plane, and parts slightly deviating from the symmetrical orientation between both twin planes, i.e., a former $(1\,0\,0)_{B2}$ plane (Schryvers and Holland-Moritz, 1998). Accurate measurements of the martensite lattice parameters, as obtained from HRTEM lattice images, indicate large local differences yielding c/a ratios ranging from 0.86, which is a normal bulk value for the present composition, to 0.95 which is extremely high and nearly yielding a cubic unit cell (Schryvers, 1999). Moreover, the microtwins of the upper-left plate are slightly curved. The latter is also visible in diffraction (not shown) and is thus a genuine structural effect and not an imaging feature.

Other peculiar features are found in some grains especially around grain boundaries from former B2 grains with relatively small orientation differences. An example of this is shown in Fig. 2b where a thin martensite plate, running from lower-left to upper-right, is seen next to a larger one extending beyond the bottom-right corner. Again strong variations in the microtwin stacking sequences are found in both plates. Moreover, it is seen that the fine twinning occurs in both grains in an alternating fashion, i.e., a fine twinning in the thin plate roughly changes over the boundary into a broad variant in the large plate and

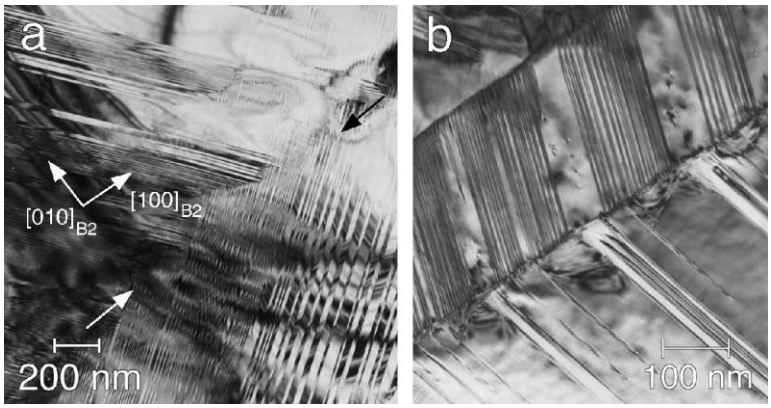

Fig. 2. Bright field TEM images of typical martensite microstructures in splat-cooled 65Ni: (a) irregular microtwin sequences and steps at interplate interface indicated by arrows (the original B2 lattice directions are also added), (b) alternating fine and broad twinning on either side of facetted interface running from lower-left to upper-right.

vice versa. In most cases these alternations are correlated with distinct steps or facets of the grain boundary. Furthermore, some dislocations are also seen in the broadest variants of the thin plate as well as some tapering of microtwins.

3.2. Melt-spun material

Fig. 3 shows the typical microstructure of as-spun 65Ni material observed at room temperature. Most of the material is transformed into the martensite phase as confirmed by SAED. Still, several untransformed B2 regions with a typical lateral size of 300 nm are present. Untransformed B2 regions occupy approximately 1/4 of the entire 65Ni material, which is in good agreement with accompanying X-ray data (Potapov et al., 2000). The SAED examination reveals that the B2 parts distributed over a large area of the sample have an identical crystallographic orientation, indicating a common crystallographic origin, i.e., a single

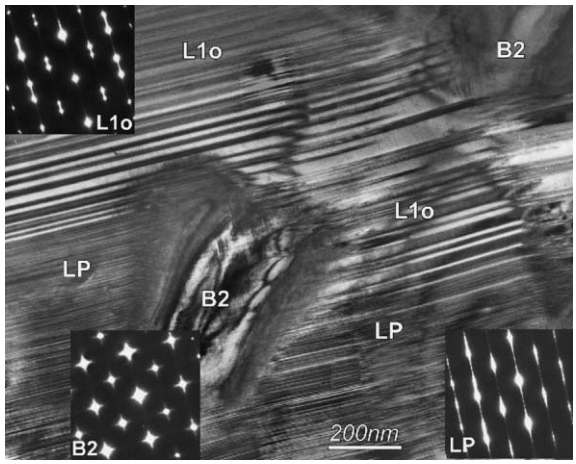

Fig. 3. Typical TEM image of nanoscale B2 regions in a martensite matrix in melt-spun 65Ni. The SAED patterns indicate twinned $L1_0$, LP microtwinned martensite and the precursor state in the B2 region.

former B2 austenite grain. Near the Bragg positions, strong $\langle 1\,1\,0\rangle_{B2}$ diffuse streaks are observed indicating that the B2 regions are in the precursor state with respect to the $\{1\,1\,0\}\ \langle 1\,-1\,0\rangle_{B2}$ shear transformation (Chakravorty and Wayman, 1976; Schryvers and Tanner, 1990). The $L1_0$ regions show the internally twinned morphology typical for Ni–Al martensite plates. Close examination of the SAED patterns reveals a faint diffuse streaking along $\langle 1\,1\,1\rangle_{L10}$ indicating the presence of multiple aperiodical $\{1\,1\,1\}\ \langle 1\,1\,0\rangle_{L10}$ stacking defects, in this case resulting in varying twin widths.

In contrast to the strictly periodical seven layered 14M structure, observed in bulk material (Martynov et al., 1983), the long period (LP) martensite in melt-spun 65Ni shows a periodicity varying between 7 and 10 layers which confirms an earlier report by Chandrasekaran et al. (1992). As a rule, this finely twinned LP structure appears nearby the untransformed B2 regions, sometimes forming an intermediate layer between the $L1_0$ and B2 structures. The $L1_0$ and LP structures can replace each other smoothly without changing the microtwin plane.

As the martensitic transformation is known to proceed by a displacive transformation mechanism, a sharp habit plane is normally observed between the parent and transformed structures. As seen from Fig. 3, conventional TEM images of interfaces between B2 and martensite in spun 65Ni are blurred usually indicating an inclined or less sharp interface. HRTEM indeed shows a gradual lattice distortion over such an interface (Potapov et al., 2000).

In order to investigate the local composition, melt-spun material was examined by precise EDX analysis. B2 regions are characterised by a Ni depleted area about twice the size as the structural B2 area, i.e., the region of lower Ni content extends to about 100 nm around the B2 precipitate. Although EDX analysis intrinsically implies a random error of ± 0.5 at.%, the present extensive statistics allows one to conclude that the B2 regions in 65Ni contain on average 1–3 at.% less Ni than the $L1_0$ (14M) matrix (Potapov et al., 2000). An additional proof of these concentration inhomogenities is provided by EELS analysis, using the Al dependency of the second sub-peak of the NiL_3 absorption peak as a relative composition measure (Potapov et al., 2000). Similarly, in 62.5Ni melt-spun material, occasional martensite plates in the austenite matrix correspond with a local increase in Ni of the same amount. It is thus concluded that these structural inhomogeneities (i.e., small regions with an atomic structure deviating from that of the matrix) originate from local composition fluctuations most probably appearing during crystallisation. Such fluctuations are known to severely affect the M_s temperature (Au and Wayman, 1972; Potapov et al., 2000; Smialek and Hehemann, 1973).

3.3. Bulk material

Martensite microstructures in cubic-to-tetragonal transformations have been documented to a great extend in the past (Chakravorty and Wayman, 1976), also including comparisons with numerical results from phenomenological theories (Baele et al., 1987; Chakravorty and Wayman, 1976). Recently, using experimental data from HRTEM images and theoretical findings from advanced continuum theories, more detail could be obtained on these matters (Ball and Schryvers, 2001).

In bulk, but also in splat-cooled samples as already seen from Fig. 2, a diversity of macrotwin boundaries is found when observing the material at the mesoscale. Indeed, as illustrated in Fig. 4, macrotwin boundaries between two microtwinned martensite plates with microtwins originating from perpendicular $(1\,1\,0)_{B2}$ and $(1\,-1\,0)_{B2}$ planes can be almost planar or they can reveal a zig-zag or wavy configuration. Without descending to the atomic level, the fine structure of all these macrotwin boundaries can be described using two basic constitutive elements. These two elements are clearly distinct and will be referred to as "crossing" type and "step" type elements. The crossings seen in Fig. 4a correspond to situations where the two plates have similar microtwin widths and the terminology refers to the fact that the deformations of one plate are seen to penetrate to some extent into the other plate. The resulting macrotwin boundary is a prior $\{1\,0\,0\}_{B2}$ plane. The steps in Fig. 4b reveal a configuration in which one set of

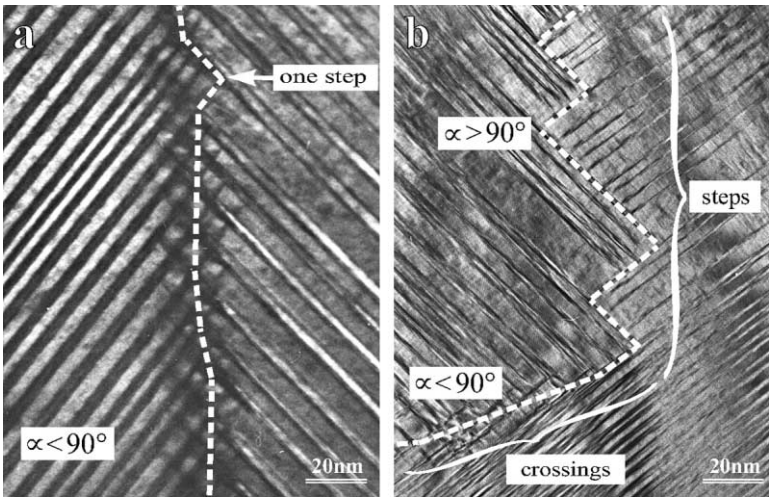

Fig. 4. Different microstructural configurations observed at macrotwin boundaries between plates with close to perpendicular microtwins: (a) crossing type between plates with stable volume fractions and (b) step type at changing microtwin widths.

microtwins ends at a twin plane of the other plate and this over a distance of several microtwins. This situation is seen to occur in cases where there is a strong but local variation in twin width on one or both sides of the interface as also seen in Fig. 2a. The single step in Fig. 4a is also found at a site where changes in the twin widths occur (finer on the left, broader on the right). Usually, the smallest twins seem to be stopped by the plate accommodating the widest twins, the latter thus providing the macrotwin interface, which is, locally, a prior $\{1\,1\,0\}_{B2}$ plane.

The combination of these two constitutive elements can explain the diversity in macrotwin boundaries observed at the mesoscale. When the crossing type boundary is dominant, the interface is ideally a prior $\{1\,0\,0\}_{B2}$ plane as in Fig. 4a. When the step type boundary is dominant, a zig-zag configuration is observed which corresponds with the alternation of $(1\,1\,0)_{B2}$ and $(1\,-1\,0)_{B2}$ planes for the interface as in the upper part of the Fig. 4b. Note that a configuration with regular alternating step sizes yields a macrotwin boundary with an average orientation again corresponding to a prior $\{1\,0\,0\}_{B2}$ plane. Finally, the combination of these two constitutive elements in a more or less random way and with differences in the width of the blocks can give wavy macrotwin boundaries or an abrupt change in the direction of the macrotwin boundary (bottom part Fig. 4b).

An alternative distinction on the mesoscale can be made by measuring the angle α between the two families of microtwin planes. Irrespective of the step or crossing nature of the macrotwin interface, angles larger or smaller than 90° have been observed, as also indicated in Fig. 4. The fact that even for a single macrotwin interface both cases can be measured providing a drastic change in orientation of the boundary, as seen in Fig. 4b, indicates that this changing orientation has some correlation with the plate growth, rather than with the original nucleation configuration. The comparison with 90° stems from the fact that the prior $\{1\,1\,0)_{B2}$ planes of these two sets of microtwin planes are perpendicular to one another. This angle will be referred to below as α.

When observing the macrotwin boundaries at high magnification and under atomic resolution conditions as in Fig. 5, it is seen that the widest microtwin variants on both sides of the interface belong to the same deformation variant, e.g., U_1. The present example corresponds with an $\alpha > 90°$ crossing case, but the same conclusion holds for $\alpha < 90°$ as well as for the step configuration. To what extent this is an intrinsic characteristic or rather due to particular choices during the TEM observations is unclear at present (only

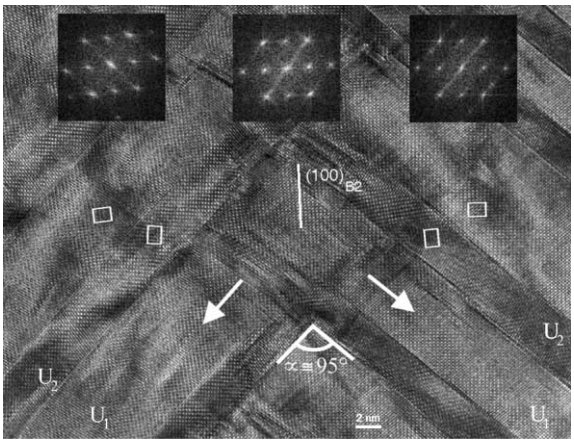

Fig. 5. HRTEM image of a crossing type macrotwin revealing local orientations of microtwin variants as well as local deformations in the central region. The power spectra are taken from the largest U_1 variants underneath the prints. The present example has $\alpha > 90°$. The arrows indicate the relative direction of shearing of the close packed planes with respect to the atomic positions in the austenite.

few interfaces can be properly investigated by HRTEM, mainly because of the need for observing along well-defined crystallographic directions). As the plates involved will be slightly rotated in opposite directions by the rigid body rotations R_i, including a component in the plane and one out of the plane, the final orientation of the similar variants will also slightly differ. For the present case where $\alpha > 90°$ the elongated axis of the largest microtwin variant is close to perpendicular to the macrotwin interface, as seen from the rectangles in Fig. 5. On the contrary, for the $\alpha < 90°$ case, this direction is close to parallel with this interface. The actually measured angles between the two families of microtwin planes differ considerably from interface to interface: values ranging from 84° to 97° have been found (Ball and Schryvers, 2001).

3.4. Crossing type boundaries

In Fig. 5 the two microtwin sequences are seen to penetrate each other so that all four twin variants are in contact and thus involved in the formation of the interface. This interface is not a sharp plane but rather a transition layer of approximately 5–10 nm wide around a prior $\{1\,0\,0\}_{B2}$ plane acting as a mirror and allowing for a gradual rotation of the atom planes from the core of one microtwin sequence into the other. This results in a mixed deformation region at the transition layer, as evidenced by the power spectra of the U_1 variants in Fig. 5, as obtained by Fourier transform of the scanned images.

The actual angle between the prior $[1\,0\,0]_{B2}$ directions in the U_1 variants on either side of the interface is observed to be 6–8°, while that for the U_2 variants is 14–16°. The observed difference between the large (U_1) and small (U_2) variants corresponds well with the rigid body rotation bringing the larger variants closer to their undeformed orientation.

Further away from the interface the microtwins are often seen to bend or reorient over a distance between 50 and 500 nm on either side. This is clear from the overviews in Fig. 6a and b (and also seen in Fig. 2a). In the first case, a discrete reorientation is observed at the trace in between the arrows, i.e., further and closer to the macrotwin interface the microtwin planes remain unrotated. In the second case, however, the microtwin planes are seen to bend gradually when approaching the macrotwin interface. Moreover, this bending is in opposite directions in the left and right parts, i.e., at $(0\,1\,0)_{B2}$ and $(1\,0\,0)_{B2}$ type interfaces, respectively. This indicates that this accommodation feature is not only related to the relative orientations of both plates involved but also to the actual macrotwin plane.

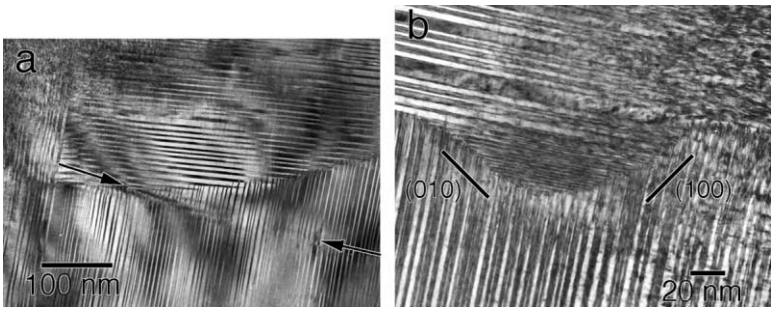

Fig. 6. Two examples of structural features accommodating stresses remaining after the coalescence of two microtwinned martensite plates: (a) discrete reorientation and (b) continuous bending.

As such a macrotwin interface involves contact regions between variants of the same type but with different rigid body rotations implied by the respective choice of microtwin orientation in each plate on either side, this interface cannot be formed as part of an overall energy minimising configuration including austenite–martensite interfaces surrounding the entire configuration (Ball and James, 1987; Bhattacharya, 1991). This is confirmed by the fact that all self-accommodating configurations embedded in austenite as well as a single in situ observation of martensite nucleation consist of all three variants and angles of 120° between the different microtwin planes (Schryvers and Holland-Moritz, 1998; Van Tendeloo and Schryvers, 1999). By the same reasoning, if such plates are forced to make contact because of the nucleation and growth process, extra stress accommodating features are expected to be observed. Still, as this accommodation will only take place after contact it will be restricted to an area relatively close to the macrotwin. The original orientation of the microtwin planes can thus still be recognised far away from the macrotwin. The angle between the two families of microtwin planes measured outside the bending regions can thus be compared with the calculation of the angle θ between the original $\{1\,1\,0\}$ plane in the austenite and the corresponding microtwin plane in the respective martensite plate

$$\cos\theta = \frac{1+\eta_3 z^2}{(1+\eta_3)z} \quad \text{with} \quad z = \sqrt{\frac{\eta_1^{-2}+\eta_3^{-2}}{2}}. \tag{1}$$

In practice, as the actual rotation axes are not exactly parallel with $[0\,0\,1]_{B2}$, the calculated values for θ have to be transformed into the net angle α between the normals n of the microtwin planes before being compared with the experimental measurements for α, as shown in the "α (from θ)" column in Table 1.

Now it can be shown (Ball and Schryvers, 2001) that if two plates with $(1\,1\,0)_{B2}$ and $(1\,-1\,0)_{B2}$ microtwin planes and with the same relative volume fractions for the U_1 and U_2 variants are forced to be compatible over a macrotwin interface, then, assuming a zero-energy continuous deformation, the macrotwin plane must either be a former $(1\,0\,0)_{B2}$ plane or a former $(0\,1\,0)_{B2}$ plane. This is an important result as it provides a rigorous argument for the observation of the $\{1\,0\,0\}_{B2}$ type interfaces, although these do not appear in the overall energy minimising configurations (Ball and James, 1987; Bhattacharya, 1991). That this reasoning is not in contradiction with the previously mentioned non-existence of such an overall energy minimising configuration, is due to the fact that now only compatibility over the central macrotwin is assumed and no surrounding austenite–martensite interfaces are taken into account. The angle α between the microtwin planes for the $(1\,0\,0)_{B2}$ case is then given by $90° + \gamma - \phi$, with

$$\tan\frac{\phi}{2} = \frac{\eta_3\rho}{\eta_1(1+\rho)} \quad \text{with} \quad \rho = \lambda\frac{\eta_3^2-\eta_1^2}{\eta_3^2+\eta_1^2}, \tag{2}$$

and for the $(0\,1\,0)_{B2}$ case by $90° - \gamma + \phi$, with

Table 1
Calculated and measured microstructural parameters based on deformation parameters $\eta_1 = 0.93$ and $\eta_3 = 1.15$ measured under the assumption of volume preservation

	γ	λ	θ	α (from θ)	$90° \mp \gamma \pm \phi$
Calculated	12.2°	0.35	2.9°	93.7°, 86.3°	+,−: 92.4°, −,+: 85.2°
Observed	12.5°	0.35	–	92–97°, 83–86°	90–95°, 83–85°

In "α (from θ)" the distinction between cases with α larger and smaller than 90° is made and measurements are made far from the interface, while for "$90° \mp \gamma \pm \phi$" the measurements are made close to the interface and separated into the $(1\,0\,0)_{B2}$ and $(0\,1\,0)_{B2}$ cases mentioned in formulas (2) and (3).

$$\tan\frac{\phi}{2} = \frac{\eta_1\rho}{\eta_3(1-\rho)} \tag{3}$$

with γ defined in Fig. 1b and λ the volume fraction of the small variant. Finally, the numerical values listed in the last column of Table 1 are obtained from theory and experiment, the latter using measures close to the interface.

Comparing the calculated and observed values for γ and λ indicates that the assumption of volume preservation is indeed valid. Although the spread in measured values for α is relatively large, the order of magnitudes are in good agreement and the directions of rotation are confirmed. Using the proper values for the deformation parameters η_1 and η_3 it is predicted that the stress accommodation close to the interface leads to a smaller deviation from the cubic 90° angle for the $\alpha > 90°$ case while it yields a larger deviation for the $\alpha < 90°$ case. However, the calculated differences between α and ϕ are relatively small, so that one wonders whether this will have an observable effect. Still, as seen from the example in Fig. 6b where $\alpha = 92°$ for the $(1\,0\,0)_{B2}$ macrotwin and 88° for the $(0\,1\,0)_{B2}$ one, this angle is decreased for both macrotwin parts when approaching the interface, confirming the predicted behaviour based on the continuum calculation for ϕ. In fact, the difference in rigid body rotations on both sides of the macrotwin implies that, in principle, no perfect zone orientation can be found to obtain good HRTEM images around the macrotwin. As many well-resolved images were obtained, this could indicate that the ϕ correction also compensates for these differences.

The large variation in measured values could possibly be related to the fact that local and possibly dynamic features that are not taken into account by the present model can play an important role in shaping the actual atomic and microstructural features of the macrotwin interfaces. Moreover, when measuring and comparing α and ϕ, it is assumed that the rotation of the lattice can be measured through the bending of the microtwins, which is overestimating ϕ as atomic step ledges are also observed to play a role in the microtwin bending (Ball and Schryvers, 2001). Also, as the measures away from the macrotwin interface originate from low magnification images in which the traces of the microtwins are only seen when their planes are not perfectly viewed edge-on, the slight but necessary misalignment will also introduce some inaccuracy and differences between measures from different images. Aside from these stress accommodation features away and close to the interface, the highly strained tips of the smaller U_2 variants as well as the averaged orientation of the U_1 parts exactly at the macrotwin interface will also accommodate remaining stresses.

3.5. Step type boundaries

The step type boundary locally involves only three microtwin variants and can be simplified to the case where one microtwin sequence meets a pure variant. The transition layer that will allow the microtwin sequence to form a coherent interface with the pure variant is restricted to this microtwin sequence while the other sequence stays almost unaffected. The orientation difference due to the different rigid body

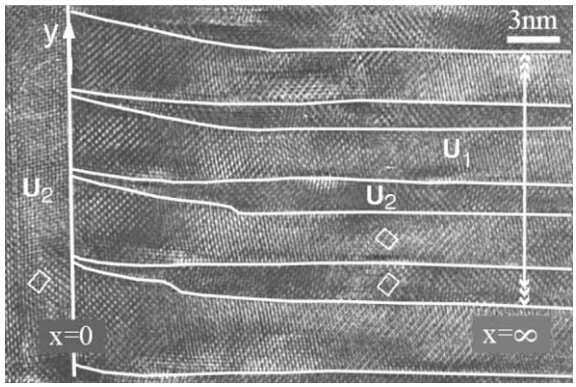

Fig. 7. HRTEM image of a step at a macrotwin interface, located on the left. The overlay lines highlight the microtwin planes. The vertical double arrow indicates the area over which the average volume fraction $\lambda(x)$ or λ_∞ is measured.

rotations on both sides, is accommodated by a local lattice deformation within this single microtwinned plate. An example of such a transition layer is shown in Fig. 7. The transition from the core of the plate on the right part of the figure to the single variant U_2 on the left starts by a bending deformation which affects both U_1 and U_2 variants. The deformation can be a pure bending or be assisted by the appearance of dislocations. Getting closer to the interface, the thinnest variant (U_2) will disappear to the benefit of the other one (U_1) through the formation of a needle structure. The disappearance of the thin variant associated with the bending deformation leads to the formation of a twin configuration between variant U_2 of one laminate and variant U_1 of the other one. Only very small lattice distortions in the left U_2 variant are observed at the sites of the incoming needles.

When limiting our measurements to situations where no dislocations are observed, a full treatment of the experimental measures yields the plot shown in Fig. 8. Here the dependence of the bending as Δy with the distance x to the macrotwin interface (as indicated on Fig. 7) and measured from HRTEM images is presented. The major influence on the precision of the measurements is that of the averaging over different planes at a given step configuration.

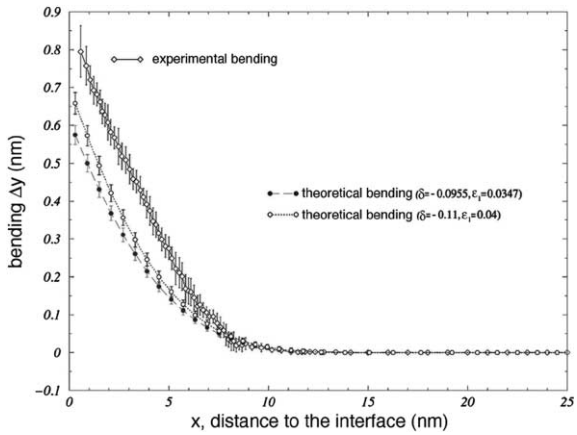

Fig. 8. Comparison between experimental measures and theoretical simulations of the bending with distance from the interface (two different deformation parameter sets were used for the latter).

Also given in Fig. 8 are the calculated values for the bending based on a 2D linear elasticity model using deformation parameters η_1 and η_3. The function is given by

$$\frac{d\Delta y}{dx} = -\frac{4|\delta|}{1+\varepsilon_1}(\lambda_\infty - \lambda(x)) \tag{4}$$

with

$$\varepsilon_1 = \frac{\eta_1+\eta_3}{2} - 1 \quad \text{and} \quad \delta = \frac{\eta_1-\eta_3}{2} \tag{5}$$

with $\lambda(x)$ the volume fraction at the position x and λ_∞ the stable volume fraction far away from the interface (Boullay et al., 2001). The uncertainty on the input values for η_1, η_3 and λ are incorporated into the theoretical curves, yielding the uncertainty flags around the calculated points. It can be seen that the position of the start of the bending as measured from HRTEM images is well reproduced by the simulations, but the amount of bending between 5 and 10 nm is slightly underestimated by the theoretical approach. Closer to the interface, however, the curvature of the graphs becomes similar indicating that in this region the behaviour of the discrete crystal lattice is well described by the present continuum model. Changing the values of η_1 and η_3 (i.e., using literature data (small open dots) (Boullay et al., 2001) or present measures from HRTEM assuming volume preservation (small full dots)) yields a slightly different curvature for the theoretical graphs.

4. Conclusions

Although the principal parameters governing the microstructure of martensite are well known, the actually observed configurations still reveal many complex phenomena that can intuitively be understood but cannot exactly be modeled as yet. These include small structural differences due to compositional and/or stress configurational inhomogeneities. A first attempt to such a modeling provides new understanding of the nano- and microstructures existing at and around macrotwin boundaries between plates with close to mutually perpendicular microtwin planes.

The use of samples prepared under different external conditions allows us to reveal and compare a range of different micro- and nanostructures. In general it can be stated that the fast quenching procedures induce less homogeneous microstructures, in composition (e.g., B2 regions in martensite plates in melt-spun ribbons) as well as in stress regimes (more irregular microtwin sequences). Such inhomogeneities will certainly affect the transformation behaviour and thus the shape memory conditions, e.g., by smearing out M_s over a broader temperature range.

Continuum theory shows that the observed macrotwin configuration cannot be formed as a self-accommodating shape, but if one is forced to form (e.g., as a result of separate growth processes) it will yield a macrotwin interface along a former {1 0 0} plane of the austenite. From the experimental images, several structural features are observed accommodating the small change in orientation needed for this configuration.

Acknowledgements

The authors like to thank K. Bhattacharya, R. James, S. Conti and S. Müller for stimulating discussions and D. Holland-Moritz and P. Ochin for the preparation of the splat-cooled and melt-spun materials, respectively. This work was supported by the European Training and Mobility Research program of the

EEC under the project FMRX-CT98-0229 (DG12-BDN) entitled "Phase Transitions in Crystalline Solids" and by the Belgian IUAP project P4/10 "Systems with Reduced Dimensionality".

References

Au, Y.K., Wayman, C.M., 1972. Thermoelastic behaviour of the martensitic transformation in β' Ni–Al alloys. Scripta Metall. 6, 1209–1214.

Baele, I., Tendeloo, G., Amelinckx, S., 1987. Microtwinning in Ni–Mn resulting from the beta to theta martensitic transformation. Acta Metall. 35, 401–412.

Ball, J.M., James, R.D., 1987. Fine phase mixtures as minimizers of energy. Arch. Rat. Mech. Anal. 100, 13–52.

Ball, J.M., Schryvers, D., 2001. The formation of macrotwins in NiAl martensite, Proceedings of IUTAM Symposium on Mechanics of Martensitic Phase Transformation in Solids, Hong Kong, 2001 (publ. Kluwer).

Bhattacharya, K., 1991. Wedge-like microstructure in martensites. Acta Metall. Mater. 39, 2431–2444.

Boullay, P., Schryvers, D., Kohn, R., 2001. Bending martensite needles in Ni65A135 investigated by 2D elasticity and HRTEM. Phys. Rev. B 64, 144105.

Chakravorty, S., Wayman, C.M., 1976. Metall. Trans. A 7, 555–582.

Chandrasekaran, M., Beyer, J., Delaey, L., 1992. Some questions on the structure of martensite and precursor in Ni(<63 at.%)–Al alloys. Scripta Metall. Mater. 27, 1841–1846.

Martynov, V.V., Enami, K., Khandros, L.G., Tkachenko, A.V., Nenno, S., 1983. Scripta Metall. 17, 1167–1173.

Otsuka, K., Ohba, T., Tokonami, M., Wayman, C.M., 1993. A new description of long period stacking order structures of martensites in beta-phase alloys. Scripta Metall. Mater. 29, 1359–1364.

Potapov, P.L., Ochin, P., Pons, J., Schryvers, D., 2000. Nanostructural characterisation of melt-spun Ni–Al material. Acta Mater. 48, 3833–3845.

Schryvers, D., 1999. Advanced TEM studies of martensite and related phase transformations. In: Koiwa, M., Otsuka, K., Miyazaki, T. (Eds.), Solid–Solid Phase Transformations (JIMIC-3), vol. 12, pp. 947–954.

Schryvers, D., 1993. Microtwin sequences in thermoelastic NixAl100-x martensite studied by conventional and HRTEM. Philos. Mag. A. 68, 1017–1032.

Schryvers, D., Holland-Moritz, D., 1998. Austenite and martensite microstructures in splat-cooled Ni–Al. Intermetallics 5, 427–436.

Schryvers, D., Tanner, L.E., 1991. EM of stress-induced martensite and pretransition microstructures in Ni62.5Al37.5. In: Liu, C.T., Kunsmann, H., Otsuka, K., Wuttig, M. (Eds.), MRS, Shape Memory Materials, vol. 246, pp. 33–38.

Schryvers, D., Tanner, L.E., 1990. On the interpretation of HREM images of premartensitic microstructures in the Ni–Al B2 phase. Ultramicroscopy 32, 241–254.

Smialek, J.L., Hehemann, R.F., 1973. Transformation temperatures of martensite in β-phase Ni–Al. Metall. Trans. 4, 1571–1575.

Van Tendeloo, G., Schryvers, D., 1999. Atomic structure of alloys close to phase transitions. In: MRS Fall Meeting, vol. 580, pp. 283–292.